

Visual Computing for Archaeological Artifacts with Integral Invariant Filters in 3D

H. Mara¹ and S. Krömer²

Heidelberg University

IWR – Interdisciplinary Center for Scientific Computing

¹ FCGL – Forensic Computational Geometry Laboratory

² vNNG – Visualization and Numerical Geometry Group

Mathematikon – Im Neuenheimer Feld 205

69120 Heidelberg, Germany

Abstract

3D-artifacts from ancient civilizations contain many different kinds of information in form of forensic trace evidence, e.g., tool marks from stylus or fingerprints on wax sealings. These very fine structures are increasingly captured by various 3D-acquisition techniques and stored as irregular meshes. We introduce filter algorithms for the processing of these datasets to finally extract meaningful information at predefined scales. Therefore, Multiscale-Integral Invariants (MSII) are introduced as robust filter methods with their four different variants, using volume, patch, surface and line integrals for their specific sensitivity on mean curvature, Gaussian curvature or noise detection. Smoothing as known from 2D-raster image processing cannot be applied directly. It needs adaptation to the irregular structure of the triangular grids describing 2D-manifolds in 3D-space. We introduce a fast 1-ring smoothing with a skillful weighting by distance and area of the neighboring points and triangles. Finally, we apply our technique to the various motivating examples for showing the results as false color images with isolines, indicating the respective field of function values, e.g., curvature in various norms or correlations in the feature space. Smooth isolines are indicators for the successful removal of noise. We finally compare the fully automated results with a manual graphic rendering of a faded handwriting found in the tomb of the empress Gisela of Swabia.

CCS Concepts

•Computing methodologies → Computer graphics; •Applied computing → Fine arts;

1. Introduction

Motivated by the continuous demand for new means of documentation for archaeological artifacts, we are developing methods and algorithms for application on Cultural Heritage objects. Nowadays, there is a multitude of high-resolution 3D-acquisition techniques available like *Structure from Motion* (SfM) [Ull79]; the principles of structured light and stereo [SM92]; *Computed Tomography* (CT) [KJM^{*}14]; *Light Detection and Ranging* (LiDAR) [SRR^{*}16]; and *Reflectance Transformation Imaging* (RTI) [WHV^{*}16]. All these techniques have rapidly increased the amount of 3D models with numerous small details. The range of digitized objects is vast – from coins and jewelery, via remains of architecture, through to traces found in the shape of landscapes [Hes14].

1.1. Cuneiform script on clay tablets

The oldest remains of script are preserved on clay tablets [Sod94] and date back more than 5000 years [BLVW17]. This includes ad-

ministrative and scientific documents, especially geometry and astronomy, rich collections of literature, e.g., the epic of *Gilgamesh*, throughout the daily affairs of ancient civilizations. They are written in cuneiform, impressed into the clay with a stylus. Cuneiform script was used throughout the centuries and in different languages in the so-called Fertile Crescent, dominated by Babylonia and Assyria. Today, only a few experts around the world are able to decipher this script and reassemble the various fragments that are distributed in famous collections and museums and still are found in excavations in the Middle East.

1.2. Medieval wax sealings

More recent documents, written on vellum, paper, etc., are usually scanned with 2D devices. However, there exist vast numbers of wax objects in archives, like sealings, which require 3D scanning. Throughout history, documents have been authenticated by seals involving officials. These sealings normally are connected through vellum ribbons with the vellum of the deed. Thousands of detached seals are stored in these archives with almost no method at hand

to analyze the original period or to reattach the seals to their documents. Similar to criminalistics in securing of evidence, the fingerprints in the backs of the wax sealings enable reconstructions of relationships.

A small number of high-resolution 3D-models of wax seals of the foundation of Heidelberg University can be found in our Computer Graphics *HeiData(verse)* (<https://heidata.uni-heidelberg.de/dataverse/iwrgraphics> – visited 20/07/2017). These datasets are published and sustainably maintained by the *Competence Centre for Research Data* of the *Heidelberg University Library*. The seals are permanently accessible, including their backsides with fingerprints, e.g., seal *UAH SG 5* [KM15]. It is free for download and also referenceable, using its *Digital Object Identifier* (DOI): [10.11588/data/10000](https://doi.org/10.11588/data/10000).

1.3. Faint inscriptions on medieval lead plates

The empress Gisela of Swabia was interred in 1043 in the grotto of Speyer Cathedral, Germany. Her tomb was opened for the first time in 1900, and a burial lead plate (619 to 625 mm width, and 388 to 412 mm height) was found amongst other burial objects. This plate is densely filled with an inscription of fourteen lines of which only four lines were carried out in the final manner. For the greatest part the preparatory scratch of the other eleven lines was still visible in 1900 as documented by the photographer Jakob Schröck on large size glass plate negatives during the archeological excavation. The Historical Museum of the Palatinate, Speyer, is in the possession of files of historical paper prints. The inscription was retraced with white ink on top of one of these paper prints for better readability.

A detail is shown in Figure 7b (unpublished), while the whole text was described in rough terms in [Gra01]. The plate is of relevance not only to determine the dedication of the Speyer Cathedral, but is also a unique example of an inscription of that period which is exactly dateable and may serve as a reference for epigraphic studies. In the tomb and for more than 850 years, there was a limited amount of oxygen, but after a hundred years of exposure to the normal atmosphere, lead oxide and carbonate encrustations now are covering the whole plate and the preparatory scratch is almost gone. Extremely shallow traces, left by the stylus of the scribe, are barely visible to the unaided eye, also hard to capture with optical scanners and almost not visible in renderings with standard computer graphics.

1.4. General processing of surfaces as irregular grids

All these applications and research questions in the humanities, based on tangible objects of Cultural Heritage, require the transformation of the acquired high-resolution 3D-data into meaningful features. Traditionally, this is achieved by ink drawings on paper, where an archaeologically skilled craftsman represents objects with lines for important features. E.g., characters, incisions and silhouettes are represented by lines, while patterns of dots denote the condition of a surface. Therefore a common challenge is to detect characteristic points, polygonal lines and connected components within triangulated irregular surfaces, i.e., piecewise linear 2D-manifolds \mathcal{M} embedded in \mathbb{R}^3 . Furthermore, a manual drawing

in its final state is typically drawn with ink for monochrome printing. This means that archaeologists often expect a binary image as a result. In this case uncertainties are neglected, which can be shown with gray scales and/or color gamut. As binarization equals segmentation, this is a well-known hard task in computer science and we provide new methods for fine and faint details on digitally acquired surfaces.

Structure of this paper

The paper is structured as follows: We start with a brief introduction of robust filtering with integral invariants where we explicitly point out our four different approaches: (i) volume integrals and (ii) patch surface integrals for their specific sensitivity on mean curvature or Gaussian curvature, and the interplay of (iii) surface and (iv) line integrals for noise detection. Thereafter we go deeper into the idea behind fast 1-ring smoothing. The linear weighting is done by means of the distance of the neighboring points and the area of the respective triangles, and with mean as well as median filter. As results we show the different applications which we motivated above, and point out the specific advantages of our algorithm that allows for fine tuning of feature extraction.

2. Related work and state-of-the-art

Geometric analysis in – and of – Cultural Heritage is a steadily advancing field with different kinds of foci from single details on single objects up to processing large collections, e.g., [GLS^{*}15]. [PPY^{*}16] provides 62 references for single object analysis and processing relevant to our work, of which 15 concern objects in the micro-scale range. For the domain of cuneiform script, there was a closely related project led by the *Lehrstuhl für Altorientalistik, University of Würzburg* [FWMC14]. While algorithms are proposed in large numbers, there are only a few software frameworks available for scientific tasks like the well-known *MeshLab* (<http://www.meshlab.net> – visited 08/08/2017) [CCC^{*}08] maintained by the *University of Pisa*, Italy.

The most recent related work was shown for carving structures, using principal curvatures and the so-called *Frangi filter* [LPTH17]. This approach uses numeric differentiation to determine the directions of the principal curvatures λ_1 and λ_2 , used to compute mean curvature and Gaussian curvature. Determining the points of the edges (ridges and valleys) is done by searching for points having $\lambda_2 \approx 0$ and $\lambda_1 \gg 0$. The latter additionally ensures to select concave areas similar to cylindric indentations, i.e., the so-called vesselness measure. Due to noise of the acquisition, damages and discretization the authors had to strongly smooth the surface using an isotropic Laplace filter. Despite the smoothing the detected valley points are scattered around centerlines of the indentations. Their experiments include user interactions applied on rather well preserved carvings. Hardly visible shallow indentations as considered in Section 1.3 are unlikely to be detected.

Integral invariants – as alternative means of curvature measure – were first introduced for robust 2D-shape matching [MCH^{*}06] and later adapted for geometry processing [PWHY09]. The big advantage of numeric integration in contrast to numeric differentiation is the absence of smoothing artifacts. Invariance against rotation is

achieved by choosing a spherical integration domain. The numeric integration is computed for each vertex of an irregular mesh where the vertices are the centers of the spherical domain. As the radius r determines the sensitivity for a feature size we have to use a range of radii to detect features of varying sizes. Sharing the vertex as domain center leads to multiple nested spheres. Choosing a maximum radius to detect the largest expected feature results in a single parameter needed for our multi-scale approach [Mar12]. The radii of the smaller spheres are equidistantly distributed between zero and the maximum radius. They depend on the number of scales n , which is computed depending on the mesh resolution and the *Nyquist-Shannon sampling theorem*. A heurisitic default value for n has proven to be sufficiently precise and computationally efficient for meshes acquired with industrial high-resolution 3D-scanners. We precompute up to four different feature spaces each of dimension n assigning up to four feature vectors to each vertex.

Within the scope of this paper we investigate distance measures in these feature spaces for visualization of characteristic surface marks. We provide the Cultural Heritage experts with a meaningful choice of measures depending on their actual objects. The given examples are representatives of the finest details, which are virtually impossible to analyze and detect with the bare eye. In case of the cuneiform script the integral invariants are actually much too sensitive for surface details. Therefore we extend our approach by an optional fast smoothing filter.

3. Multi-scale filtering with integral invariants

We define integral invariants using an indicator function $\mathbf{1}$ for local integration within a sphere \mathbb{S} . It encloses a ball B centered at a point \mathbf{p} of a discrete two-dimensional manifold \mathcal{M} . This manifold describes the surface of an object and encloses a volume $\mathbf{1}_{\mathcal{M}}$. Note that the border $\partial\mathbf{1}_{\mathcal{M}}$ is the manifold \mathcal{M} itself. The first integral invariant for a scale r in \mathbb{R}^3 is

$$V_r = \int_{B_r(\mathbf{p})} \mathbf{1}_{\mathcal{M}} dx dy dz. \quad (1)$$

In a similar manner three further integral invariants can be defined. Using the \cap as an intersection of volumes ($B, \mathbf{1}_{\mathcal{M}}$) and surfaces (\mathbb{S}, \mathcal{M}) a total of four domains for integration can be defined:

\cap	B	:	\mathbb{S}
$\mathbf{1}_{\mathcal{M}}$	\mathbb{V}	:	\mathcal{S}
\mathcal{M}	\mathcal{P}	:	\mathcal{L}

(2)

Computing the volume $V = |\mathbb{V}|$, surface patch area $P = |\mathcal{P}|$, partial sphere area $S = |\mathcal{S}|$ and line length $L = |\mathcal{L}|$ we get four different curvature measures. V and S are related to *Gaussian curvature*, having a signed finite range of values which is typically normalized to $[-1, 1]$. $V < 0$ means concave and $V > 0$ means convex. P and L are relatives of the mean curvature, having an unsigned infinite range of values $[0, \infty]$, where normalized values below 1 indicate a sharp tip. Larger values indicate increasing roughness which, e.g. can be introduced by noise of the acquisition. The extreme case of ∞ exists when a fractal surface is enclosed by the

sphere. Figure 1 illustrates the quadruple of integral invariants in \mathbb{R}^3 .

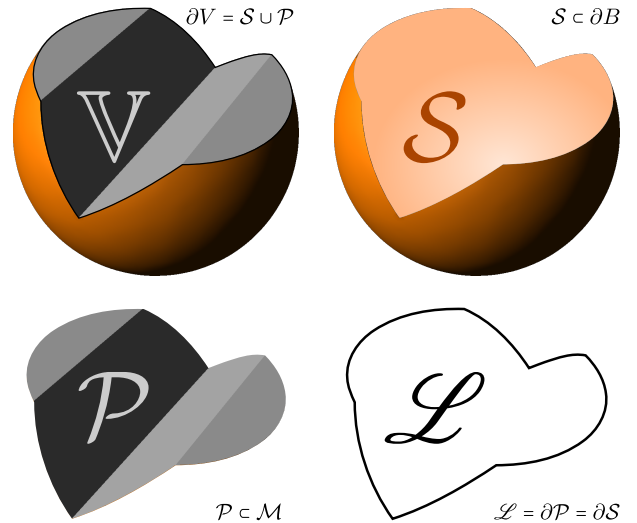


Figure 1: Graphic representation of the quadruple of integral invariants in \mathbb{R}^3 . Top-left shows the enclosed volume \mathbb{V} having the surface $\mathcal{B} \cup \mathcal{S}$ as border $\partial\mathbb{V}$. These two surfaces are shown top-right and bottom-left, and share the line \mathcal{L} as common border in the bottom-right.

For visualization purposes V is most significant for computing the most meaningful high-contrast images used for further studies of an object by an expert. Additionally, it is very useful for segmentation and feature extraction because its relation to *Gaussian curvature* for means of distinction between concave, convex and flat surface areas. The segmentation results can be improved using P to suppress false-positives as shown for raster images using the *Dual Integral Invariants* (DII) algorithm [Mar16]. S and L are useful to determine and suppress noise.

Figure 2a shows a high-resolution 3D-dataset of the backside of a medieval sealing and traces of fingerprints in the wax. These traces were left, when the sealing was attached to a document with a ribbon covered by wax. As there exist tens of thousands of such sealings in archives, we can expect to match at least some of the fingerprints, which will establish additional personal links between documents. Furthermore, fingerprints in 3D are also found on ancient objects made from clay, either unintentionally [MKJB10] or knowingly functioning as a signature of the manufacturer. Figure 2b shows the integral invariant filter response V using a single $r = 0.04 \text{ mm}$ clearly revealing the fingerprints. Figure 2c shows $P_{0.04}$, indicating the roughness of the surface.

Using a range of radii r leads to *Multi-Scale Integral Invariants* (MSII) which are implemented within the *GigaMesh* Software Framework (<http://gigamesh.eu> – visited 07/08/17) [MKJB10].

Another implementation can be found as part of the *LiVT* toolbox (<http://sourceforge.net/projects/livt> – visited 20/07/17) for analyzing *Digital Terrain Models* (DTMs) [Hes14]. Having a set of radii r_j , we get a feature

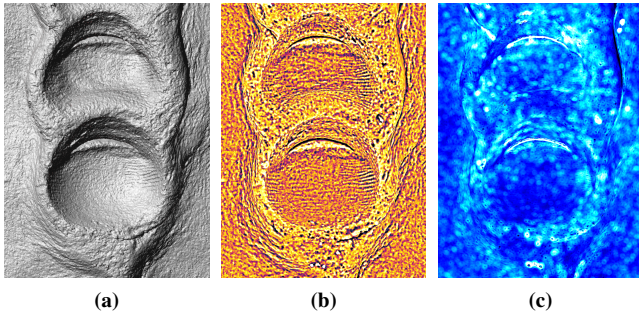


Figure 2: Backside of a 14th century sealing of the Holy Roman Emperor Charles IV, Inventory No. 7 at the Hessian State Archives in Marburg, Germany: (a) Manifold with virtual illumination, (b) volume based integral invariant filter response V_r and (c) surface based integral invariant filter response P_r using a radius of $r = 0.04\text{ mm}$.

vector for each point $\mathbf{p}_i \in \mathcal{M}$, using filter responses normalized by the size of the ball B

$$\mathfrak{V}_i = (\hat{V}_1, \dots, \hat{V}_j, \dots, \hat{V}_n)^T \quad \text{with} \quad \hat{V}_j = \frac{V_j}{|B_{r_j}|}, \quad (3)$$

which spans an n -dimensional feature space, using the first integral invariant. For practical application $n \approx 8$ or 16 has proven useful. The smallest equidistant radii r_n/n should be larger than the shortest edge within the mesh. According to the *Nyquist–Shannon sampling theorem* and [MKS09], the largest radius r_n has to be larger than the largest feature to be detected.

In previous work, we treated \mathfrak{V}_i like an independent feature vector, neglecting the fact that it is actually a feature function. The elements \hat{V}_j always depend on the previous element \hat{V}_{j-1} as the volume of a smaller ball is always part of a larger one – like onion-skins. Although we neglected this fact by applying various metrics for independent vectors, e.g. p -norms, cosine similarity and correlation methods, we have achieved appealing high-contrast visualizations, which were helpful for applications by improving the readability of weathered inscriptions [Krö13].

However, segmenting \mathcal{M} into connected components \mathcal{C} , representing meaningful features like cuneiform characters was not user friendly in terms of, e.g. pinpointing a single threshold with a *Graphical User Interface* (GUI) like it is done in *GigaMesh* selecting a reference vector \mathfrak{V}_i for color mapping using a metric. One solution would have been the use of multiple selection and/or dynamic thresholds.

3.1. Dependencies within the quadruple of feature vectors

As the elements of the feature vectors ($\mathfrak{V}, \mathfrak{P}$), based on the volume V and surface patch area P , are dependent, we decided to improve our approach by weighting the feature vectors accordingly, when computing distances within the feature spaces. Note that the other two possible feature vectors ($\mathfrak{S}, \mathfrak{L}$), which are computed using the area of the sphere segments S and the length of the line of intersection L from Equation 2, do not have any dependency at all.

The difference between scale dependency of integral invariants is shown for the dependent surface integral invariant $P_i = |\mathcal{P}_i|$ and the independent line integral invariant $L_i = |\mathcal{L}_i|$ in Figure 3. Between the scales the integral invariant \hat{S} has an independency like \hat{L} , whereas \hat{V} has a similar dependency like \hat{P} .

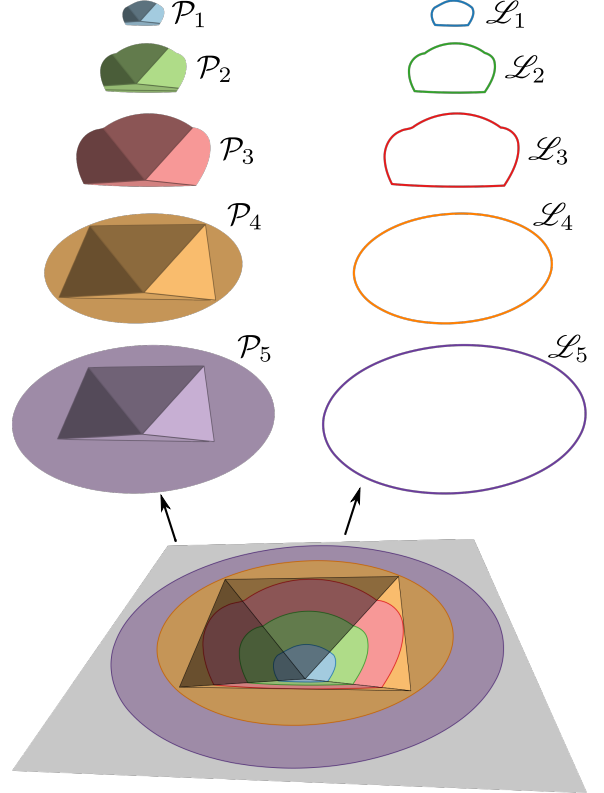


Figure 3: Example for the scale dependency of the surface integral invariant $P_i = |\mathcal{P}_i|$ with $\mathcal{P}_1 \subset \mathcal{P}_2 \subset \dots \mathcal{P}_5$ and the scale independent line integral invariant $L_i = |\mathcal{L}_i|$.

Therefore we choose to (re-)use the most prominent p -norms with $p = 1, 2, \infty$, which have proven themselves suitable for visualization purposes. The weight of each element of \mathfrak{V}_i is computed as the amount of volume independent of all previous scales:

$$w_j = \frac{|B_{r_j}| - |B_{r_{j-1}}|}{|B_{r_n}|} = \frac{r_j^3 - r_{j-1}^3}{r_n^3} \quad \forall j \in \{1, \dots, n\} \quad (4)$$

Note that $r_0 = 0$ for consistency. With equidistant radii

$$\Delta r = r_j - r_{j-1} = \frac{r_j}{n} = \text{const.} \quad (5)$$

we can easily (pre-)compute all weights by the number of scales n :

$$\mathbf{w} = \frac{1}{n^3} \left(j^3 - (j-1)^3 \right) \quad \forall j \in \{1, \dots, n\}. \quad (6)$$

Note, that for large n we can detect numeric errors $\varepsilon > 0$

$$\varepsilon = 1 - \sum_{j=1}^n \mathbf{w}. \quad (7)$$

By componentwise multiplication of \mathbf{w} with all \mathfrak{V}_i , we account for the dependencies and improve the visualization.

In a similar manner we can improve the 2-norm by adapting the *Mahalanobis distance* D_M between two (random) vectors \mathbf{x} and \mathbf{y}

$$D_M(\mathbf{x}, \mathbf{y}) = \sqrt{(\mathbf{x} - \mathbf{y})\mathbf{S}^{-1}(\mathbf{x} - \mathbf{y})^T}, \quad (8)$$

where \mathbf{S} is the covariance matrix, which equals the identity matrix \mathbf{I} for the 2-norm. If \mathbf{I} is weighted by the covariance of each dimension, we can compute a normalized 2-norm. As larger scales depend on smaller scales, we can use Equation 6 to model a weight matrix \mathbf{W} describing this dependency having the elements

$$w_{j,k} = \frac{3j^2 - 3j + 1}{k^3} \quad \forall j \in \{1, \dots, k\} \text{ with } k \in \{1, \dots, n\}. \quad (9)$$

All other elements of the rectangular matrix \mathbf{W} below the main diagonal are zero, because smaller scales do not depend on larger scales. The weight matrix \mathbf{W}^P for \mathfrak{P} are computed using the area $|\mathbb{S}^2|$ of the 2-dimensional circle disc

$$w_{j,k}^P = \frac{2j - 1}{k^2} \quad \forall j \in \{1, \dots, k\} \text{ with } k \in \{1, \dots, n\}. \quad (10)$$

The weight matrices \mathbf{W}^S and \mathbf{W}^L for \mathfrak{S} and \mathfrak{L} are the identity matrix \mathbf{I} as there is no dependency for S and L .

Figure 7 in the next section shows an application with a detail of the faint part of an unfinished inscription. Figure 7f shows the visualization using the ∞ -norm in comparison to Figure 7h based on the weighted ∞ -norm. Figure 7g shows the *Mahalanobis*-inspired result using

$$f(\mathbf{p}_i) = \sqrt{(\mathfrak{V}_j - \mathbf{o})\mathbf{W}(\mathfrak{V}_j - \mathbf{o})^T} \quad \forall \mathbf{p}_i \in \mathcal{M} \quad (11)$$

in contrast to the 1-norm, which resulted in a better contrast than the 2-norm. \mathbf{o} is either the origin, which corresponds to ideal flat surfaces within the feature space spanned by \mathfrak{V} . $f(\mathbf{p}_i)$ is a generic function value (scalar) attached to each of the vertices of the mesh, which is typically exported as quality field in the open *Stanford Polygon* (PLY) format.

3.2. Fast 1-ring smoothing

In our high-resolution meshes with dense vertices of several hundred points per mm^2 we see noise propagating within the results of the MSII filter. This noise becomes visible when isolines of the field of function values $f(\mathbf{p}_i)$ are rendered, and it becomes visible in jagged outlines for connected components of segmented areas of interest.

The design principles for filtering of function values in irregular grids are the same as for those well-known algorithms used for raster images. However, they require adaptation as there is no fixed distance between the points and no fixed number of neighboring points in 1-rings of irregular grids.

In the following we proceed solely the 1-ring neighborhood of all points of \mathcal{M} considering the center of a 1-ring as $\mathbf{p}_0 \in \mathcal{M}$. Although the number n of the elements in each 1-ring might differ, it is always indexed by $i \in \{1, \dots, n\}$ in a clockwise direction.

The smallest edge length within the 1-ring around the vertex \mathbf{p}_0

$$\Delta_{\min}(\mathbf{p}_0) := \min_{i=1}^n (|\mathbf{p}_i - \mathbf{p}_0|) \quad (12)$$

is shortly denoted by Δ_{\min} and becomes the radius of the so-called geodesic disc. Figure 4 shows a typical configuration of an 1-ring, its geodesic disc with radius Δ_{\min} and triangles \mathbf{t}'_i used for weighting.

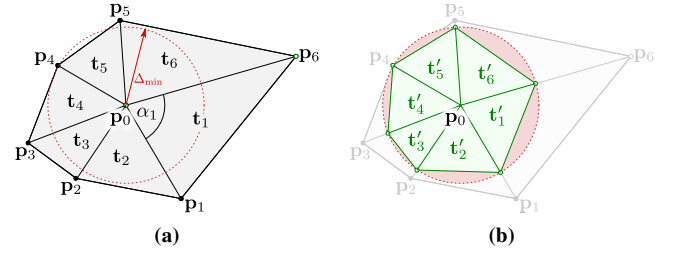


Figure 4: 1-ring with (a) irregular triangles \mathbf{t}_i and the geodesic disc with radius Δ_{\min} . Here $\Delta_{\min} = |\mathbf{p}_4 - \mathbf{p}_0|$, indicated as the red arrow. (b) Approximation of the disc with an interpolated 1-ring of triangles \mathbf{t}'_i having an area of A'_i .

The function values f'_i at the respective points \mathbf{p}_i along this disc are interpolated by

$$f'_i := f_0 + \Delta_{\min} \frac{f_i - f_0}{|\mathbf{p}_i - \mathbf{p}_0|} \quad (13)$$

where f_0 is the function value of \mathbf{p}_0 . Note that $0 < \frac{\Delta_{\min}}{|\mathbf{p}_i - \mathbf{p}_0|} \leq 1$ such that the new f'_i is always a weighted mean of f_0 and f_i by the distance of the respective points. For the weighted mean of the function value $f_i^t/3$ at each triangle \mathbf{t}'_i we compute

$$\begin{aligned} f_i^t &:= f_0 + f'_i + f'_{i+1} \\ &= 3f_0 + \Delta_{\min} \left(\frac{f_i - f_0}{|\mathbf{p}_i - \mathbf{p}_0|} + \frac{f_{i+1} - f_0}{|\mathbf{p}_{i+1} - \mathbf{p}_0|} \right). \end{aligned} \quad (14)$$

So far we used the distance to the central point \mathbf{p}_0 as weight function, but we also have to consider the distance of the points \mathbf{p}_i to their neighbors \mathbf{p}_{i+1} in the 1-ring. We do this by computing the relative area of the geodesic disc marked by the three points $\mathbf{p}_0, \mathbf{p}_i$ and \mathbf{p}_{i+1} . Instead of circle segments we approximate the geodesic disc by triangles \mathbf{t}'_i achieving faster computation. As all those triangles are isosceles having two edges of constant length Δ_{\min} we can compute their weight as the area of the isosceles triangle \mathbf{t}'_i using the Pythagorean theorem

$$A'_i := |\mathbf{t}'_i| = \frac{|\mathbf{p}_{i+1} - \mathbf{p}_i|}{4} \sqrt{4\Delta_{\min}^2 - |\mathbf{p}_{i+1} - \mathbf{p}_i|^2}. \quad (15)$$

Regarding Figure 4a, the angle α_i could as well be used for weighting, computing $A'_i = \sin(\alpha_i)\Delta_{\min}^2$, which is equivalent to Equation 15. But it is computationally expensive due to the $\sin(\cdot)$ operation and the numeric error is visible when the result of the mean filtering is rendered as color per vertex. Furthermore, computing Δ_{\min} within each 1-ring will cause tremendous amounts of redundant computing operations. Therefore we define $\overline{\Delta_{\min}} := \min\{\Delta_{\min}(\mathbf{p}_0) \mid \mathbf{p}_0 \in \mathcal{M}\}$ as the shortest edge for all triangles of the mesh. We will

use this $\overline{\Delta_{\min}}$ in all the above computations. This will increase the computing speed by a factor of ≈ 10 .

For a 1-ring we now compute the weighted mean function value with the total area $A = \sum_{i=1}^n A'_i$ as

$$\tilde{f}_0 := \frac{\sum A'_i f_i^t}{3A} \quad \forall i \in \{1, \dots, n\} \quad (16)$$

with a negligible error due to the 1-ring approximation of the geodesic disc.

For a 1-ring weighted median filter instead, we can use all equations except 16, which is replaced by a list of pairs (f_i^t, A'_i) sorted by f_i^t . The area $\frac{A'_i}{A}$ is again used as a weight such that $1 = \sum_{j=1}^n \frac{A'_j}{A}$.

The weighted median now becomes

$$\tilde{f}_0 = \frac{f_k^t}{3} \quad \text{satisfying} \quad \sum_{i=1}^{k-1} \frac{A'_i}{A} < \frac{1}{2} \leq \sum_{k+1=1}^n \frac{A'_i}{A}. \quad (17)$$

For the special case that $\frac{1}{2} = \sum_{k+1=1}^n \frac{A'_i}{A}$, which should not be excluded but rarely occurs, we compute $\tilde{f}_0 = \frac{f_k^t + f_{k+1}^t}{6}$.

4. Results for high-resolution 3D-datasets

Especially for high-resolution 3D-measurement data, we have hundreds of vertices per mm^2 , which means strong oversampling for slightly larger features like cuneiform script. This could be overcome by the application of a mesh reduction algorithm, leading to the *chicken or the egg* question, because relevant features have to be detected before thinning the mesh to preserve meaningful details.

Therefore the 1-rings and the geodesic ring radius $\overline{\Delta_{\min}}$ are typically extremely small and f_0 in Equation 14 becomes very dominant. Computing larger geodesic rings is computationally very expensive as it has $O(n^2)$ complexity by definition. With improvements like *binary space partitioning* (BSP) and bit-arrays for addressing larger neighborhoods of triangles we could reduce the complexity to $O(n \log n)$ for computing the integral invariants.

However, an algorithm to compute larger geodesic discs still would involve tremendous amounts of slow operations to access the main memory to collect and process all the necessary triangles. This decelerates the smoothing of function values of high-resolution meshes far beyond an interactive use in magnitudes of minutes to hours. As an alternative we propose a repetitive application of our fast 1-ring smoothing using either the mean or the median variant shown above.

Figure 5 shows a small portion of cuneiform tablets as a typical example, where we have to detect more than 20 wedges within an area of $\approx 60 mm^2$ described by 67.000 vertices. The manually marked wedges are shown in orange color in Figure 5b as an overlay to the high-contrast rendering in Figure 5a virtually using metallic surface properties for the original clay surface. Especially the hatched red triangle is severely damaged and has a faint overlap with the large vertical wedge. Within the group of three

wedges left to the damaged part it appears that one wedge was either imprinted twice or its outline was deformed while imprinting the wedge above.

Figure 5c shows the correlation of feature vectors, which is combined with the auto-correlation in Figure 5e as suggested in previous publications [MKJB10]. In this – and many other cases – the segmentation and extraction as *Scaleable Vector Graphics* (SVGs) propose in [MK13] for further processing with machine learning algorithms [BGM15] will result in serrated outlines, leading to unfeasible skeletons. This is shown by the isolines, computed by using the MSII filter results and their (auto-)correlation. To outline possible segmentation results, we show on-the-fly computed isolines, using the filter results stored as $f(\mathbf{p}_i)$.

The repeated application of the mean filter $\tilde{f}_{\times 30}(\mathbf{p}_i)$ improves the results. The serrations of the isolines with correlation are shown in Figures 5d. The combination of correlation with auto-correlation and repeated mean filter is shown in 5f. In spite of the large numbers (≈ 30) of repetitions the filtering is achieved within seconds as intermediate results can be precomputed and reused. The results of the median filter \tilde{f} are not shown as they are very similar in their rendered representation. Differences are only numerically determinable and visible in very large magnifications. Like its common implementation for raster images, the iso-lines or contour-lines have slightly more serrations than the result of the mean filter.

Besides, or additionally to the fast 1-ring smoothing, we can apply the various distance measures with and without weights as introduced in Section 3.1 and shown in Figure 6. This figure displays the filter result for the most prominent p -norms, inducing, e.g., the Manhattan distance with $p = 1$ in Figure 6a and the Euclidean distance with $p = 2$ in Figure 6c. Their weighted variants, using Equation 6, are shown in Figure 6b for $p = 1$, Figure 6d for $p = 2$. Additionally Figure 6e shows the Mahalanobis-inspired distance based on Equation 11. It provides the best compromise in terms of smooth outlines for segmentation, which retains parts like the damaged wedge and the faint overlap with the large vertical wedge. Finally 6f for $p = \infty$ shows a weighted supremum distance and is no longer preserving the faint overlap. Combinations of those distance measurements, i.e., metrics and fast smoothing yield further improvements.

A most recent example with an important impact on history was the processing of the lead plate buried with the empress *Gisela* shown in Figure 7. Thanks to a chance find in the archive, we have got a ground truth after processing the 3D-data, which is a one-hundred-year-old photograph of a manual tracing of the plate in a much better condition. However, the manual tracing is only accurate in terms of letters, but not their representation, which is important for paleographic research.

The difference in the arrangements of the lines of the letters become visible by comparison of the 1900 photograph in Figure 7b and the modern tracing in Figure 7d. The latter was done using (image) layers of the other metrics. Furthermore, a (local) height map is shown in Figure 7c. This map was computed using a best-fit plane for this snippet.

Visualization of the feature vectors now explicitly shows the sensitivity of the method which becomes apparent compared to

the acquired and virtually illuminated gray surface in Figure 7a, and the height map in Figure 7c. Using the Manhattan distance, i.e., the 1-norm as displayed in Figure 7e, or the maximum elements, i.e., ∞ -norm displayed in Figure 7f the letters become visible. In this case the Mahalanobis-inspired approach shown in Figure 7g is also clearer than the previous visualizations of the same feature vectors, but here the ∞ -norm weighted according to the dependency of the elements between the scales shown in Figure 7h makes better use of the full range of colors.

With the assistance of our present day 3D-visualizations and the sources from the excavation the inscription was reconstructed in large parts [KUA18].

5. Summary

Within this paper we have shown two examples for processing *Script in 3D*. The most prominent examples are the cuneiform tablets, providing humanities' scholars with a vast corpus of original sources of several millenia of history. Those tablets require robust and fast filtering to digitally grasp the high density of this writing system. The relatively modern inscription on a lead plate acts as representative for all the faded and faint inscriptions, which can gain new meaning by revealing lost details using reliable algorithms.

The presented core methodology are the Multi-Scale Integral Invariants. Those exist in quadruples and provide high-dimensional feature spaces consisting of feature vectors which are actually feature functions. In addition to their relation to Gaussian and mean curvature, we could determine different properties like the amount of dependencies between scales. Therefore vectors and matrices for weighting were defined to improve the filter results shown as (i) high-contrast visualization with isolines leading to (ii) improved segmentation of irregular triangular grids. A second improvement is the application of a fast 1-ring median and mean filter mimicking a larger filter mask by repeated application. With this fast iterative filtering method, the accumulated noise of the original surface, errors of measurement and discretization artifacts can be suppressed.

6. Outlook

As a 1-ring has notable performance benefits for the mean and median filter, the next step is an adaptation of other filtering techniques. Improvements in the numeric quality of repetitive filtering are expected by using an analytically more precise computation of the geodesic disc, which has to be tailored carefully to maintain the performance. Further improvements are expected by incorporating arising computational methods based on topology, which always had strong – but sometimes forgotten – useful relations for computational geometry. In terms of application, we expect a growing number of digital objects in high-resolution beyond archaeological artifacts especially in the *Galleries, Libraries, Archive and Museum* (GLAM) domain.

Acknowledgements

This work is partially funded by the *Maßnahme 5.4 – Zukunfts-konzept* (institutional strategy) of the 2nd *German University Excellency Initiative*. Furthermore we thank our colleagues in the

humanities for fruitful discussions and access to the respective objects: (i) *Gisela*: Sabine Kaufmann, Historical Museum of the Palatine, Speyer; Matthias Untermann, *Institut für Europäische Kunstgeschichte* (IEK), Heidelberg University; Lenelotte Möller, Speyer, Germany; (ii) *Charles IV*: Francesco Roberg, Hessian State Archives in Marburg, Germany; and (iii) all past and present members of the *Assur-Forschungsstelle* and the *Uruk-Warka Sammlung* in Heidelberg.

References

- [BGM15] BOGACZ B., GERTZ M., MARA H.: Character retrieval of vectorized cuneiform script. In *Proc. of the Int. Conf. on Document Analysis and Recognition (ICDAR)* (Nancy, France, 2015). [doi:10.1109/ICDAR.2015.7333777](https://doi.org/10.1109/ICDAR.2015.7333777). 6
- [BLVW17] BÖTTNER M., LIEB L., VATER C., WITSCHEL C. (Eds.): *5300 Jahre Schrift*. Wunderhorn, Heidelberg, Germany, 2017. 1
- [CCC*08] CIGNONI P., CALLIERI M., CORSINI M., DELLEPIANE M., GANOVELLI F., RANZUGLIA G.: MeshLab: an Open-Source Mesh Processing Tool. In *Italian Eurographics Conf.* (2008), pp. 129–136. [doi:10.2312/LocalChapterEvents/ItalChap/ItalianChapConf2008/129-136](https://doi.org/10.2312/LocalChapterEvents/ItalChap/ItalianChapConf2008/129-136). 2
- [FWMC14] FISSELER D., WEICHERT F., MÜLLER GW. G., CAMMAROSANO M.: Extending Philological Research with Methods of 3D Computer Graphics Applied to Analysis of Cultural Heritage. In *Proc. 12th Eurographics Workshop on Graphics and Cultural Heritage* (Darmstadt, Germany, 2014), pp. 165–172. [doi:10.2312/gch.20141314](https://doi.org/10.2312/gch.20141314). 2
- [Gra01] VON GRAUERT H.: Die Kaisergräber im Dome zu Speyer. Bericht über ihre Öffnung im August 1900, 1901. URL: <http://publikationen.badw.de/023391026>. 2
- [GLS*15] GREGOR R., LAMPRECHT A., SIPIRAN I., SCHRECK T., BUSTOS B.: Empirical Evaluation of Dissimilarity Measures for 3D Object Retrieval with Application to Multi-feature Retrieval. In *Proc. 13th International Workshop on Content-Based Multimedia Indexing (CBMI’15)* (2015). [doi:10.1109/CBMI.2015.7153629](https://doi.org/10.1109/CBMI.2015.7153629). 2
- [Hes14] HESSE R.: Geomorphological Traces of Conflict in High-Resolution Elevation Models. *Applied Geography* 46 (1 2014), 11–20. [doi:10.1016/j.apgeog.2013.10.004](https://doi.org/10.1016/j.apgeog.2013.10.004). 1, 3
- [KJM*14] KARL S., JUNGBLUT D., MARA H., WITTUM G., KRÖMER S.: Insights into manufacturing techniques of archaeological pottery: Industrial X-ray computed tomography as a tool in the examination of cultural material. *UCL Qatar Series in Archaeology and Cultural Heritage* 1 (2014), 253–262. [doi:10.5339/uclq.2014.cas.ch27.1](https://doi.org/10.5339/uclq.2014.cas.ch27.1)
- [KM15] KRÖMER S., MARA H.: Seal of the University of Heidelberg - Siegel UAH SG 5. online / Open Access, 4 2015. [doi:10.11588/data/10000](https://doi.org/10.11588/data/10000). 2
- [Krö13] KRÖMER S.: Neue Methoden zur besseren Lesbarkeit mittelalterlicher Grabsteine am Beispiel des Heiligen Sands in Worms. In *Die SchUM-Gemeinden Speyer - Worms - Mainz*, Heberer P., Reuter U., (Eds.). Schnell & Steiner, 2013, pp. 167–188. 4
- [KUA18] KEDDIGEIT J., UNTERMANN M., AMMERICH H. (Eds.): *Pfälzisches Klosterlexikon*, vol. 4 of *Handbuch der pfälzischen Klöster und Kommenden*. Bezirksverband Pfalz, Institut für pfälzische Geschichte, 2018. 7
- [LPTH17] LAWONN K., PREIM B., TROSTMANN E., HILDEBRANDT K.: Visualization and Extraction of Carvings for Heritage Conservation. *IEEE Transactions on Visualization and Computer Graphics* 23 (1 2017). [doi:10.1109/TVCG.2016.2598603](https://doi.org/10.1109/TVCG.2016.2598603). 2
- [Mar12] MARA H.: *Multi-Scale Integral Invariants for Robust Character Extraction from Irregular Polygon Mesh Data*. PhD thesis, Heidelberg University, 2012. [doi:10.11588/heidok.00013890](https://doi.org/10.11588/heidok.00013890). 3

- [Mar16] MARA H.: Made in the Humanities: Dual Integral Invariants for Efficient Edge Detection. *it – Information Technology: Methods and Applications of Informatics and Information Technology* 58, 2 (1 2016), 89–96. [doi:10.1515/itit-2015-0037](https://doi.org/10.1515/itit-2015-0037). 3
- [MCH*06] MANAY S., CREMERS D., HONG B.-W., YEZZI JR. A. J., SOATTO S.: Integral Invariants for Shape Matching. *IEEE Transactions on Pattern Analysis and Machine Intelligence* 28, 10 (October 2006), 1602–1616. [doi:10.1109/TPAMI.2006.208](https://doi.org/10.1109/TPAMI.2006.208). 2
- [MK13] MARA H., KRÖMER S.: Vectorization of 3D-Characters by Integral Invariant Filtering of High-Resolution Triangular Meshes. In *Proc. of the Int. Conf. on Document Analysis and Recognition (ICDAR)* (Washington DC, USA, 2013), IEEE, pp. 62–66. [doi:10.1109/ICDAR.2013.21](https://doi.org/10.1109/ICDAR.2013.21). 6
- [MKJB10] MARA H., KRÖMER S., JAKOB S., BREUCKMANN B.: GigaMesh and Gilgamesh - 3D Multiscale Integral Invariant Cuneiform Character Extraction. In *Proc. VAST Int. Symp. on Virtual Reality, Archaeology and Cultural Heritage* (Paris, France, 2010), A. Artusi et. al., (Ed.), Eurographics Association, pp. 131–138. [doi:10.2312/VAST/VAST10/131-138](https://doi.org/10.2312/VAST/VAST10/131-138). 3, 6, 9
- [MKS09] MEINE H., KÖTHE U., STELLDINGER P.: A Topological Sampling Theorem for Robust Boundary Reconstruction and Image Segmentation. *Discrete Applied Mathematics (DGCI Special Issue)*, 157, 3 (2009), 524–541. [doi:10.1016/j.dam.2008.05.031](https://doi.org/10.1016/j.dam.2008.05.031). 4
- [PPY*16] PINTUS R., PAL K., YANG Y., WEYRICH T., GOBBETTI E., RUSHMEIER H.: A Survey of Geometric Analysis in Cultural Heritage. *Computer Graphics Forum* 35, 1 (8 2016), 4–11. [doi:10.1111/cgf.12668](https://doi.org/10.1111/cgf.12668). 2
- [PWHY09] POTTMANN H., WALLNER J., HUANG Q.-X., YANG Y.-L.: Integral Invariants for Robust Geometry Processing. *Computer Aided Geometric Design* 26, 1 (January 2009), 37–60. [doi:10.1016/j.cagd.2008.01.002](https://doi.org/10.1016/j.cagd.2008.01.002). 2
- [S92] SABLATIC R., MENARD C.: Stereo and Structured Light as Acquisition Methods in the Field of Archaeology. In *Mustererkennung '92, 14. DAGM-Symposium Dresden* (1992), Fuchs S., Hoffmann R., (Eds.), Springer, pp. 398–404. [doi:10.1007/978-3-642-77785-1_52](https://doi.org/10.1007/978-3-642-77785-1_52). 1
- [Ull79] ULLMAN S.: The Interpretation of Structure from Motion. *Proceedings of the Royal Society B* 203, 1153 (1979), 405–426. [doi:10.1098/rspb.1979.0006](https://doi.org/10.1098/rspb.1979.0006). 1
- [SRR*16] VON SCHWERIN J., RICHARDS-RISSETTO H., REMONDINO F., SPERAD M. G., AUERE M., BILLENE N., LOOSE L., STELSONF L., REINDEL M.: Airborne LiDAR acquisition, post-processing and accuracy-checking for a 3D WebGIS of Copan, Honduras. *Journal of Archaeological Science: Reports* 5 (2 2016), 85–104. [doi:10.1016/j.jasrep.2015.11.005](https://doi.org/10.1016/j.jasrep.2015.11.005). 1
- [Sod94] VON SODEN W.: *The ancient Orient: an introduction to the study of the ancient Near East*. Wm. B. Eerdmans Publishing Co., 1994. [doi:10.1163/1568533952663459](https://doi.org/10.1163/1568533952663459). 1
- [WHV*16] WATTEEUW L., HAMEEUW H., VANDERMEULEN B., DER PERRE A. V., BOSCHLOOS V., DELVAUX L., PROESMANS M., BOS M. V., GOOL L. V.: Light, shadows and surface characteristics: the multispectral Portable Light Dome. *Applied Physics A* 122, 976 (10 2016), 1–7. [doi:10.1007/s00339-016-0499-4](https://doi.org/10.1007/s00339-016-0499-4). 1

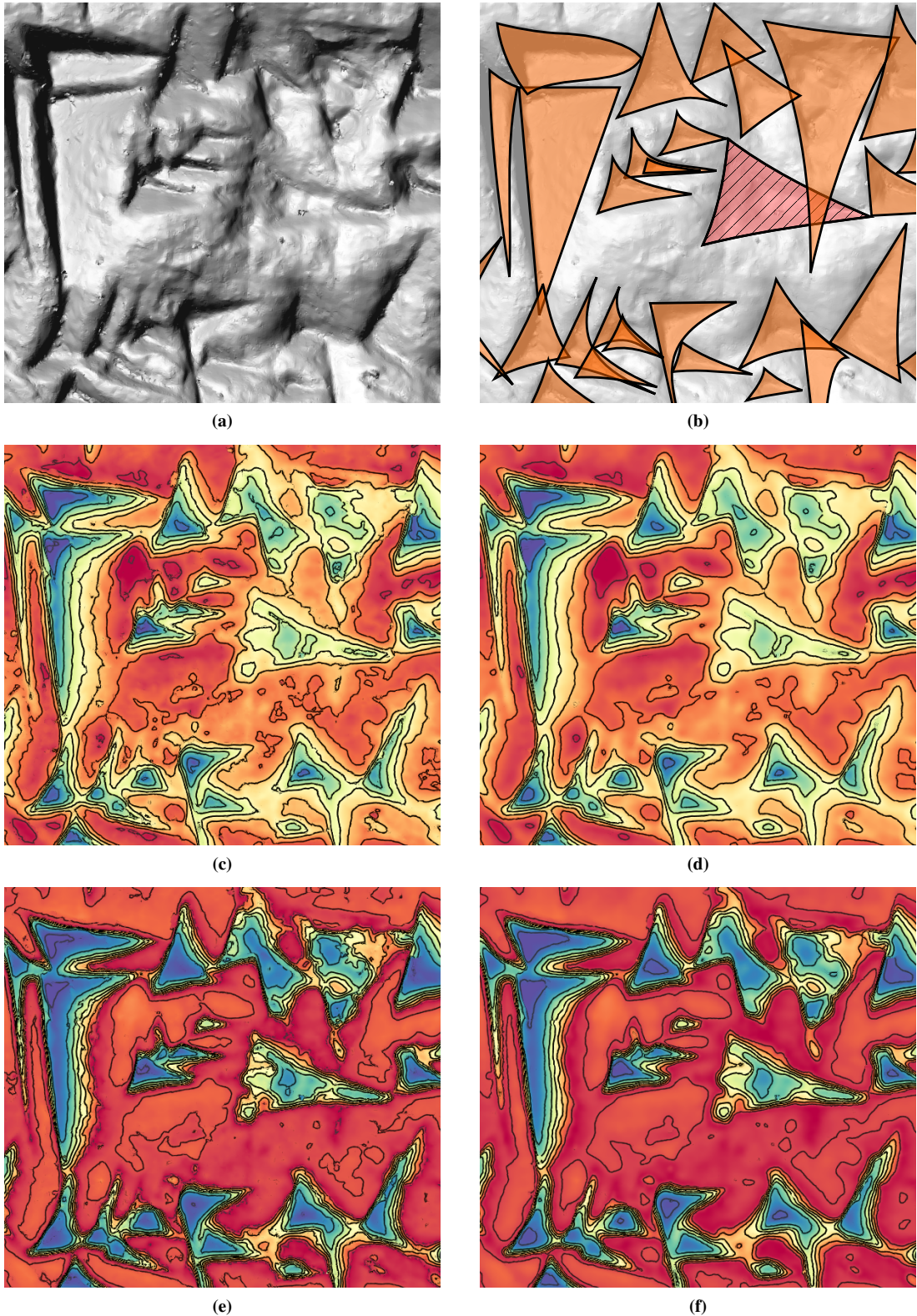


Figure 5: Small detail of a cuneiform tablet in 3D having a bounding box of $8 \times 5.5 \times 1.8$ mm described by 67000 vertices: (a) virtual high-contrast illumination, (b) manually annotated wedges including a damaged wedge, shown in red color with hatches, (c) correlation of feature vectors, combined with (e) auto-correlation as suggested in [MKJB10], (d,f) results for 30 repetitions of the mean filter $\bar{f}_{\times 30}(\mathbf{p}_i)$ for the respective filters on the left-hand side in (c,e).

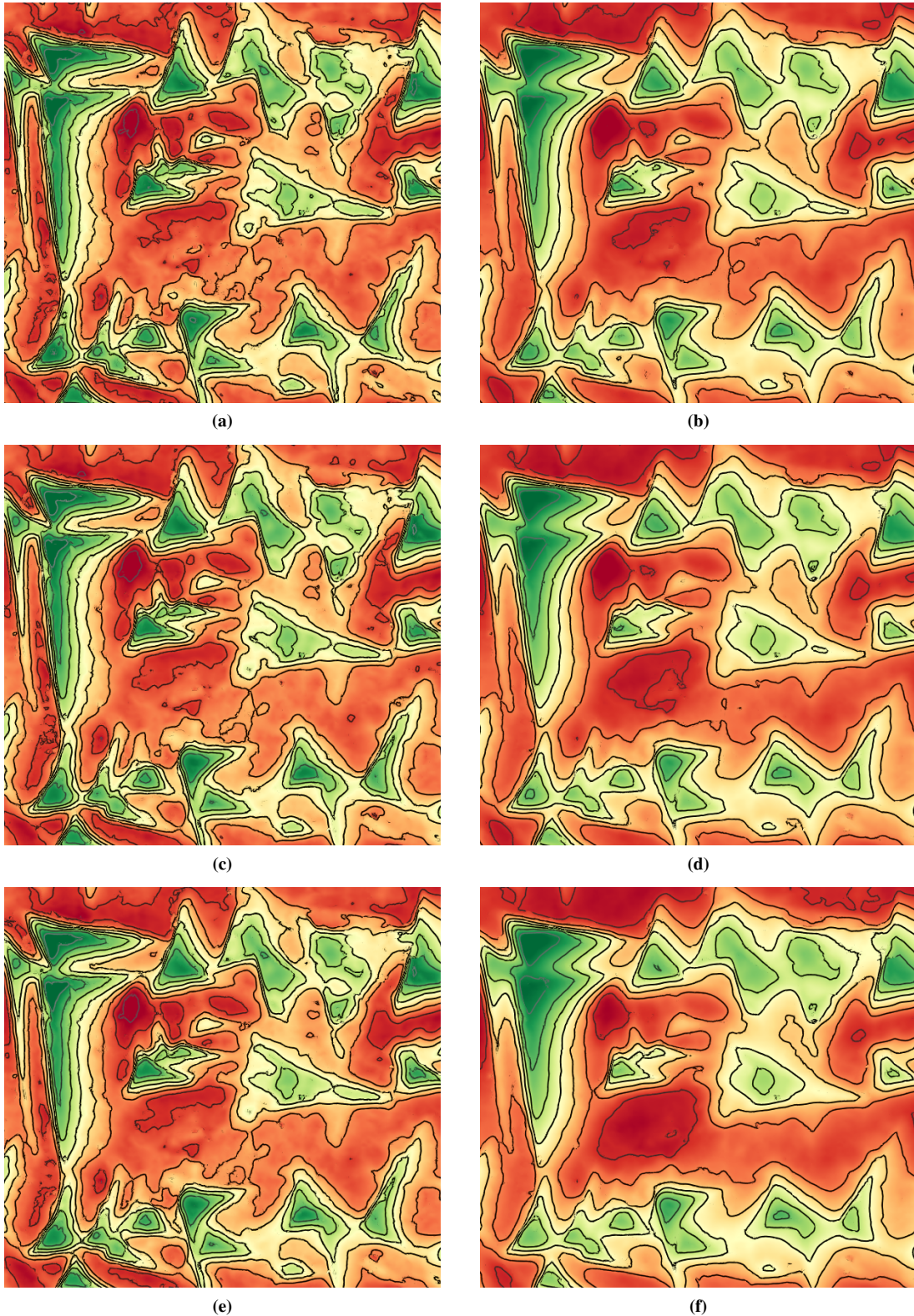


Figure 6: Cuneiform detail of Figure 5 with non-weighted (a) Manhattan distance, (c) Euclidean distance, (e) Mahalanobis-inspired distance (left column). In the right column are the (b) weighted Manhattan distance, (d) weighted Euclidean distance and (f) weighted ∞ -norm. For all distances, the volume based feature vectors Ω_i were used, given a reference at the deepest point of a well preserved wedge.

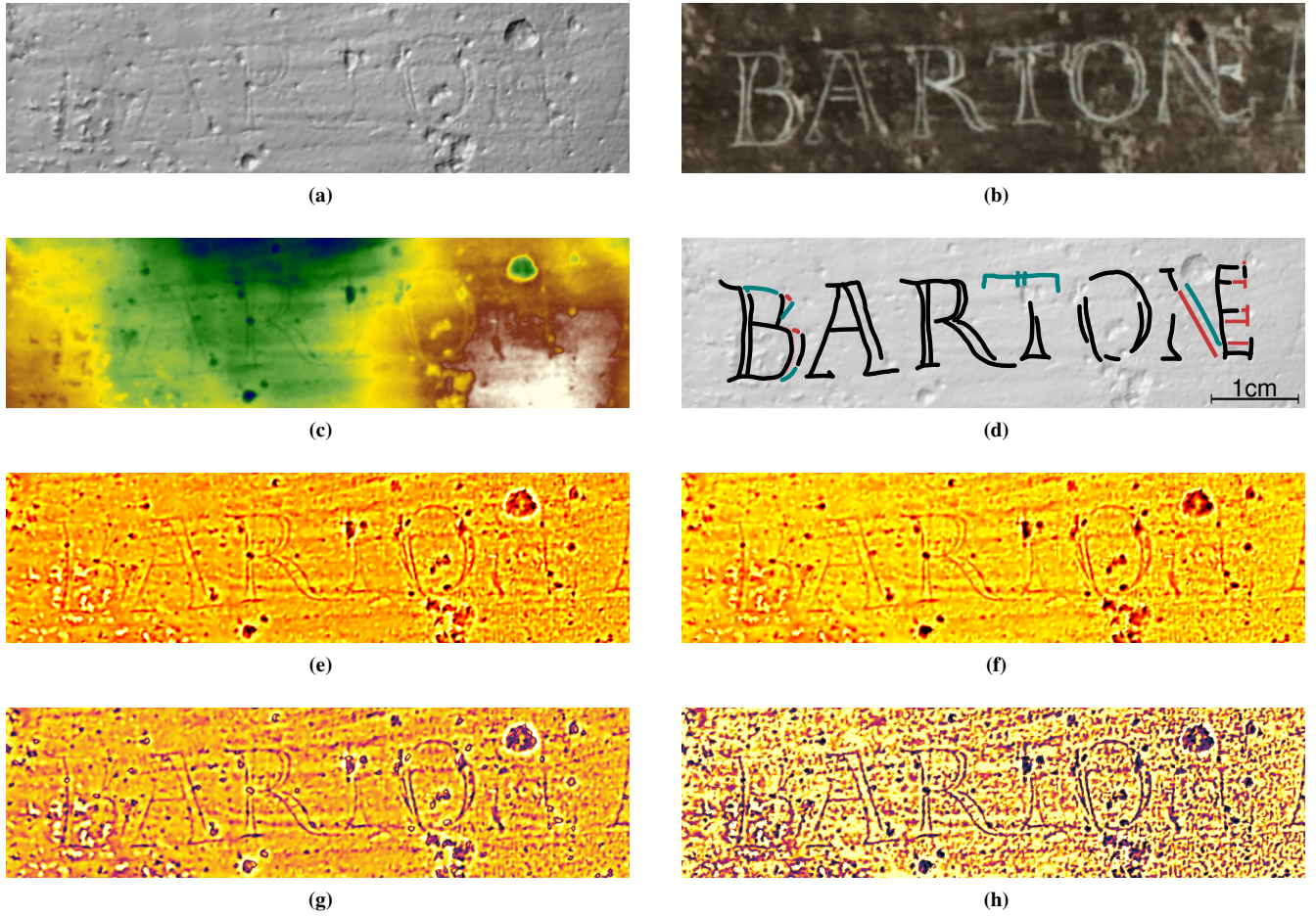


Figure 7: Detail of the 11th century lead plate, found in the tomb of empress Gisela of Swabia in the Speyer Cathedral, Germany. (a) Virtually illuminated surface and (b) ink tracing on the photograph from 1900. (c) Heightmap using a best-fit plane; the height difference between dark blue and white is 1.6mm. (d) Modern manual tracing, based upon the following MSII visualizations. Visualization of the feature vectors using their (e) Manhattan length, i.e., 1-norm and (f) maximum elements, i.e., ∞ -norm, (g) Mahalanobis-inspired approach and (h) the ∞ -norm weighted according to the dependency of the elements between the scales.